Particle tracking during Ostwald ripening using time-resolved laboratory x-ray microtomography

T. Werz[a,*], M. Baumann[a], U. Wolfram[b,1], C. E. Krill III[a]

[a] *Ulm University, Institute of Micro and Nanomaterials, Albert-Einstein-Allee 47, 89081, Germany*
[b] *University Hospital Ulm, Institute of Orthopaedic Research and Biomechanics, Helmholtzstraße 14, 89081, Germany*

Abstract

Laboratory x-ray microtomography is investigated as a method for obtaining time-resolved images of microstructural coarsening of the semisolid state of Al-5 wt% Cu samples during Ostwald ripening. Owing to the 3D imaging capability of tomography, this technique uniquely provides access to the growth rates of individual particles, thereby allowing not only a statistical characterization of coarsening—as has long been possible by conventional metallography—but also enabling quantification of the influence of local environment on particle boundary migration. The latter information is crucial to understanding growth kinetics during Ostwald ripening at high volume fractions of the coarsening phase. Automated image processing and segmentation routines were developed to close gaps in the network of particle boundaries and to track individual particles from one annealing step to the next. The particle tracking success rate places an upper bound of only a few percent on the likelihood of segmentation errors for any given particle. The accuracy of particle size trajectories extracted from the time-resolved tomographic reconstructions is correspondingly high. Statistically averaged coarsening data and individual particle growth rates are in excellent agreement with the results of prior experimental studies and with computer simulations of Ostwald ripening.

*Corresponding author; Tel: +49 731 5025372; Fax: +49 731 5025488
Email address: thomas.werz@uni-ulm.de (T. Werz)
[1] Current address: University of Bern, Institute for Surgical Technology and Biomechanics, Stauffacherstr. 78, 3014 Bern, Switzerland

Preprint submitted to Materials Characterization

Keywords: Ostwald ripening, x-ray microtomography, image segmentation

1. Introduction

As the resolution of x-ray tomography has improved from the millimeter to the submicrometer range, the scope of applications for this nondestructive 3D imaging technique has broadened from its early use in medical diagnostics to increasingly widespread employment as a tool for characterizing the complex internal microstructures of materials [1, 2]. Tomography is particularly well suited to the study of multiphase materials, as differences in local x-ray absorption can be exploited to map the spatial extent of individual phase regions—even when the latter are interconnected in a complex manner in three dimensions [3, 4]. Previously, such information could be gleaned only from a destructive technique like serial sectioning [5]; however, with the advent of high-resolution x-ray tomography, such studies no longer require cutting open the sample, thereby making it feasible to observe the evolution of phase boundaries during protracted mechanical and/or thermal processing [6–10].

This *in situ* 3D imaging capability makes x-ray microtomography ideally suited to the investigation of *Ostwald ripening,* a coarsening phenomenon first studied more than a century ago [11] and still of technological relevance today because of its prevalence during the synthesis and processing of modern multiphase materials [12–15]. In the simplest case of particles of one phase dispersed in a matrix of a second phase, Ostwald ripening manifests itself through the growth of larger particles at the expense of smaller ones, leading to an increase in the mean particle size $\langle R \rangle$ as the total number of embedded particles decreases (Figure 1). The driving force for this process is the excess energy of interphase boundaries, the overall area of which is reduced when the volume of the embedded (coarsening) phase is concentrated in fewer particles of larger size.

The first widely accepted analytic model for Ostwald ripening was proposed in 1961 by Lifshitz, Slyozov [16] and Wagner [17]. The so-called LSW model makes three primary predictions regarding the asymptotic kinetics of particle coarsening in a two-phase mixture:

(i) The cubed mean particle radius $\langle R \rangle^3$ of a given phase grows as a linear function of time t.

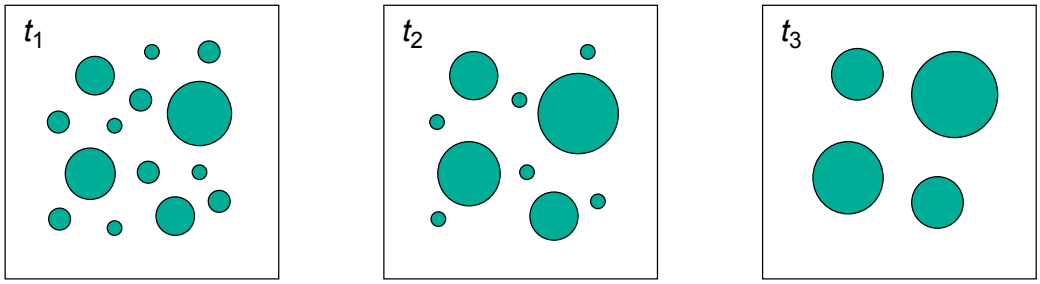

(a) (b) (c)

Figure 1: Schematic illustration of the Ostwald ripening of particles of one phase embedded in a matrix consisting of a different phase. Larger particles grow at the expense of smaller particles by atomic diffusion from the latter to the former through the matrix. This leads to an increase in the mean particle size $\langle R \rangle$ with time ($t_1 < t_2 < t_3$) without changing the volume fraction V_V of the coarsening phase.

(ii) The particle size distribution takes on a time-independent shape when normalized by the corresponding mean particle radius $\langle R \rangle$.

(iii) The quantity $R^2 \mathrm{d}R/\mathrm{d}t$, which is proportional to the instantaneous growth rate of a particle of size R, depends linearly on $R/\langle R \rangle - 1$, entailing particle shrinkage for $R < \langle R \rangle$ and growth when $R > \langle R \rangle$.

Strictly speaking, the LSW results were derived in the limit of a vanishing volume fraction of the coarsening phase (*i.e.* $V_V \to 0$), which is equivalent to the assumption of no overlap of the concentration depletion zones surrounding the shrinking/growing particles [12, 18, 19]. This assumption leads to discrepancies between theory and experiment at higher, technologically relevant values for V_V [20, 21]. Over the past six decades, numerous attempts have been made to extend the LSW model to higher volume fractions by taking particle-particle interactions into account, at least in a mean-field sense [18, 22–26]. For example, Glicksman *et al.* [24] and Wang *et al.* [26] developed a "diffusion screening theory" to describe multiparticle systems in the range $0 < V_V < 0.3$, and Marsh and Glicksman [23] established the concept of a "statistical field cell" that is valid for volume fractions up to 0.6. At still higher values for V_V, however, all current approaches to modeling Ostwald ripening begin to break down [27].

In order to guide the development of analytic models for Ostwald ripening in the high-V_V regime, it is necessary to measure the effect of particle-particle interactions on the rate of growth in each particle size class R and to assess

their dependence on the overall volume fraction V_V of the coarsening phase. Such information can be obtained only from a nondestructive 3D imaging technique that is able to map out the local environment of each particle in a real coarsening system and to deliver relevant data for quantifying the influence of that environment on the particle's growth kinetics. In this work we demonstrate that absorption-contrast x-ray microtomography meets both of these criteria. Moreover, we show that the necessary characterization capabilities are not exclusive to the specialized instrumentation found at synchrotron beamlines: the latest generation of laboratory x-ray tomographs affords sufficient intensity and resolution for performing such studies, as well.

In Section 2, we describe the sample preparation and tomographic characterization protocol that was followed to investigate Ostwald ripening in a two-phase system with $V_V = 0.74$ during both long-term (LT) and short-term (ST) annealing series. By tracking individual particles over several annealing steps, according to the approach presented in Section 3, we extract particle growth/shrinkage trajectories and compare them to statistical measures for the evolution of the ensemble of particles, discussing the results in the context of prior experimental and theoretical studies of Ostwald ripening. Finally, in Section 4 we assess uncertainties in the microstructural data obtained by this approach, considering not only experimental factors but also the consequences of segmentation artifacts on the accurate tracking of particles from one tomographic reconstruction to the next.

2. Material and methods

The aggregate state of the phases in a polycrystalline metal undergoing Ostwald ripening can be solid-solid [15] or solid-liquid [21]. Solid-liquid systems offer the advantage of minimizing the interfacial stresses between matrix and coarsening phases [28], thereby eliminating at least one factor having the potential to interfere with conventional coarsening kinetics [20]. Furthermore, ripening occurs faster in solid-liquid systems, owing to the higher rate of atomic diffusion through a liquid than a solid, thereby shortening the annealing time needed to induce a measurable change in the microstructure.

For these reasons, we chose to study a high-purity Al-5 wt% Cu alloy in the semisolid state at temperatures above the solidus line (~ 560°C). Prior to annealing, the alloy was cold-rolled to a thickness reduction of 50% and homogenized at 500°C for 24 hours in air. Samples were then cut by spark erosion into cylinders 4 mm in length and 4 mm in diameter. Tomographic

scans were recorded at a resolution of 2 µm (voxel side length) for the LT series measurements (2.42 µm for the ST series) using a cone-beam SkyScan 1172 laboratory microtomograph (Bruker microCT) operated at a source voltage of 100 kV and a source current of 100 µA. During each measurement, a total of 567 (LT) or 551 (ST) projections was recorded at an exposure time per projection of 6500 ms (LT) or 4100 ms (ST). All tomographic reconstructions were generated using filtered back-projection of the x-ray absorption images.

The experimental protocol consisted of sequential repetitions of a tomography scan performed at room temperature (Figure 2(a)) followed by a sample annealing treatment carried out in air at 630°C (Figure 2(b)). To estimate the time required for specimen heating and cooling, we mounted a thermocouple ($\varnothing$ 0.5 mm) in a hole bored into a test sample and placed the latter in an oven preheated to 630°C. It took approximately 150 seconds for the sample center to equilibrate with its surroundings; the semisolid state was reached after 100 seconds. Following removal from the oven, the sample cooled down to room temperature within 160 seconds, of which only 10 seconds were needed to exit the semisolid state. At 630°C, we estimated the volume fraction of the solid phase to be $V_V = 0.69$ for thermodynamic equilibrium between the solid and liquid by applying the lever rule to the phase boundaries indicated in the Al-Cu binary phase diagram [29]. The liquid (matrix) phase at this temperature has a significantly higher Cu concentration than the solid, coarsening phase (11 wt% *vs.* 1.5 wt%).

Upon cooling to room temperature, the matrix phase solidifies to a eutectic mixture of the Al(Cu) terminal solid solution and the intermetallic phase Al_2Cu (Figure 2(a)) [30]. Owing to the higher Cu concentration in regions formerly occupied by the liquid matrix, they absorb x-rays more strongly than do the coarsening particles, thereby enabling the matrix phase to be mapped out by absorption-contrast tomography. Unfortunately, the boundaries of the coarsening particles are not always perfectly revealed by this procedure: in some cases, the liquid wetting layer is too thin to detect (Figure 2(a)), or dewetting may have occurred during cooling, in which case there is a driving force for the liquid phase to retreat into the triple junctions. These phenomena have already been reported in Al-Cu [31] as well as in other semisolid systems, including Fe-Cu [32] and Al-Sn [33]. In these cases the imposition of a simple thresholding criterion on the gray scale of a tomographic reconstruction yields a partially marked network of particle boundaries. Complete segmentation of the characterized sample volume—*i.e.*

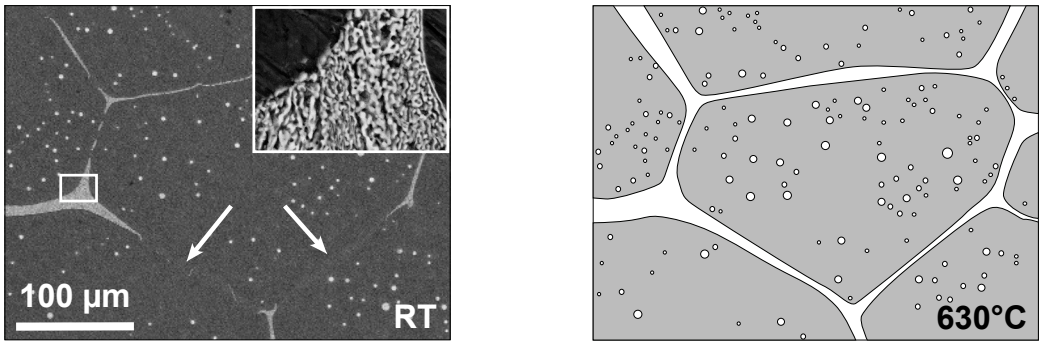

(a) (b)

Figure 2: Partially marked particle boundaries and microstructural changes during cooling. (a) Scanning electron microscopy image of Al-5 wt% Cu at room temperature (RT), revealing the presence of incompletely marked particle boundaries (arrows) as well as small spherical inclusions within the particles. The inset shows a magnified view of the Al(Cu)-Al_2Cu eutectic mixture located within the white box. Dark gray regions correspond to the Al(Cu) phase, and light gray pixels arise from Al_2Cu. (b) Schematic illustration of the semisolid state present at 630°C; here, the white regions correspond to the liquid phase surrounding the gray-shaded solid particles.

the quantitative extraction of all particle sizes and shapes—therefore necessitates carrying out additional image processing steps to close any remaining gaps in the mapping of the liquid phase.

2.1. Image processing and segmentation

Owing to its demonstrated applicability to foam-like network structures [34], we employed the watershed transformation to segment the tomographic reconstructions of Al-5 wt% Cu. Processing of the latter was carried out using the *Image Processing Toolbox* in MATLAB, and 3D visualizations were generated with the imaging software AVIZO. In order to prepare reconstructions for the watershed transformation, we removed noise and improved contrast by applying, in sequence, an adaptive Wiener filter, an edge-preserving, anisotropic diffusion filter[2] [35] and a top-hat filter to 2D slices (oriented with normal vector parallel to the symmetry axis of the sample cylinder); a typical result of these steps is shown in Figure 3(a). Imposing a threshold, we ob-

[2]Anisotropic Diffusion using ANISODIFF2 by Daniel Lopes, Matlab Central File Exchange, May 14, 2007.

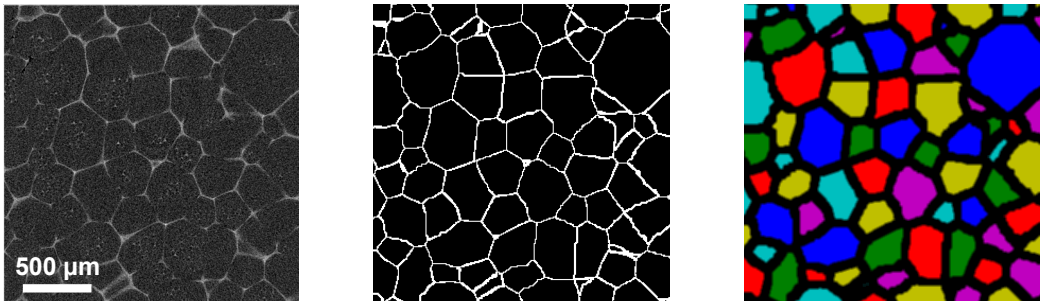

(a) (b) (c)

Figure 3: The main steps in image processing and segmentation, illustrated for a 2D section through a 3D tomographic reconstruction of Al-5 wt% Cu. (a) Image from the raw reconstruction, containing noise, precipitates of the matrix phase and partially marked particle boundaries. (b) Result following application of the watershed transformation, showing closure of gaps in the matrix-phase network. (c) Fully segmented microstructure, with individual particles labeled by arbitrarily chosen colors.

tained a binary dataset containing the partially marked network of particle boundaries.

In order to ensure reliable functioning of the watershed algorithm, it was necessary to remove spherical precipitates of the matrix phase embedded within the coarsening particles (Figures 2(a) and 3(a)). Moreover, since no particle growth or shrinkage ensues upon atomic diffusion across inclusions, they should be excluded when calculating the volume fractions relevant to Ostwald ripening. Direct analysis of tomographic reconstructions revealed that spherical inclusions make up approximately 17% of the matrix phase, independent of annealing time; the remaining matrix phase must, therefore, occupy 26% (rather than 31%) of the overall sample volume. Consequently, we take $V_V = 0.74$ to represent the "effective" volume fraction of the coarsening phase during Ostwald ripening.

Processing of 3D datasets was feasible only after downscaling by a factor of two in each dimension. The final step in preparation for the watershed transformation was the application of a 3D Euclidean distance transformation [36], which assigns a number to each voxel that is proportional to the given voxel's distance from the matrix phase (*i.e.* from the network of particle boundaries). In the two-dimensional case, the result can be interpreted as a topographic map in which the lowest-number voxels represent the peaks of hills (the particle boundary network) and the highest-number voxels denote

the deepest points in valleys (usually located near particle centers). After smoothing out local minima to avoid oversegmentation, we applied the watershed transform to the distance transform, thereby closing the voids in the reconstruction of the matrix phase (Figure 3(b)).

Once the gaps in the particle boundaries had been eliminated, we adjusted the volume fraction of the matrix phase to $V_V = 0.74$ by uniformly widening the boundaries to a value between 12 µm and 24 µm, depending on the average particle size. At this point, each remaining (*i.e.* non-boundary) voxel belongs unambiguously to exactly one particle in the sample, making it possible to determine the spatial extent of each particle and to label the latter with a unique number. Figure 3(c) illustrates the final result for a single 2D slice passing through a cylindrical sample.

Any particle touching the surface is deleted from the segmentation, as surface particles lack a full complement of neighboring particles, which is likely to have an effect on the local kinetics of growth. For each remaining particle, we calculate its equivalent radius R as the radius of a sphere of equal volume. If the latter is smaller than $R_{\min} = 15\,\mu\text{m}$, we remove the corresponding particle from the segmentation, owing to the non-negligible likelihood that such a small region has arisen from noise in the reconstruction. (At a voxel side length after downsampling of 4 µm for the LT series, our choice of cutoff value for $R_{\min}$ corresponds to an equivalent diameter of only 7.5 voxels, compared to a matrix-phase thickness of 3 to 6 voxels.)

2.2. Data collection

Samples were subjected to two distinct annealing protocols in order to access different regimes of microstructural evolution during Ostwald ripening (Table 1). A long-term (LT) annealing series was designed to reveal global parameters, such as the growth exponent and the steady-state shape of the particle distribution. Six samples were repeatedly characterized tomographically at annealing times ranging from 1 to 63 h at 630°C. Short-term (ST) annealing intervals only 1 h in duration were applied at the same temperature to three samples in order to extract the growth rates of individual particles using the particle-tracking algorithm described in the next section. Prior to the initial tomographic scan, the ST samples were annealed for 3, 7 or 15 h to establish different starting average particle sizes.

Table 1: Long-term (LT) and short-term (ST) annealing series for samples of Al-5 wt% Cu. Entries in the table indicate the cumulative time spent by a given sample at 630°C prior to tomographic characterization at room temperature.

series name	annealing time (hours)																			
LT1–6	1	3				7					15								31	63
ST1		3	4	5	6	7														
ST2						7	8	9	10	11										
ST3											15	16	17	18	19					

2.3. Sample alignment and particle tracking

An unavoidable consequence of carrying out the annealing treatments in an external oven rather than inside the microtomograph itself are changes in sample alignment from measurement to measurement. These changes manifest themselves in translational and rotational offsets when comparing reconstructions of the same specimen at two different annealing times (Figure 4(a))—a situation that exacerbates the difficulty of tracking the evolution of individual particles during the short-term annealing series. The misalignment between segmentations at times t_{i-1} and t_i of the same ST annealing sequence was corrected in a stepwise manner, starting with a determination of the translational offset along the x, y and z directions of the sample centroid. After removal of the centroid offset (Figure 4(b)), the rotational offset about the z-axis was determined from the location of a prominent surface notch created during spark erosion. Relative rotations with respect to the x and y-axes were determined from the offset between sample centroids in 2D sections passing through the top and bottom layers of each specimen reconstruction. Following correction for all three sample tilts, superposition of the t_{i-1} and t_i datasets revealed excellent agreement between the reconstructed sample surfaces (Figure 4(c)). The associated rotation and tilting of interior voxels resulted in relative changes of less than 0.05% in the calculated mean particle radius and below 0.1% in the radii of individual particles.

Once the sample misalignment has been eliminated, we can proceed with the task of identifying the same particle in reconstructions recorded at different annealing times. Since particles progressively disappear during Ostwald ripening but never nucleate, we know that each particle still present at the longest annealing time must also be found at all earlier times. Consequently, we developed a particle-tracking algorithm starting from the final annealing

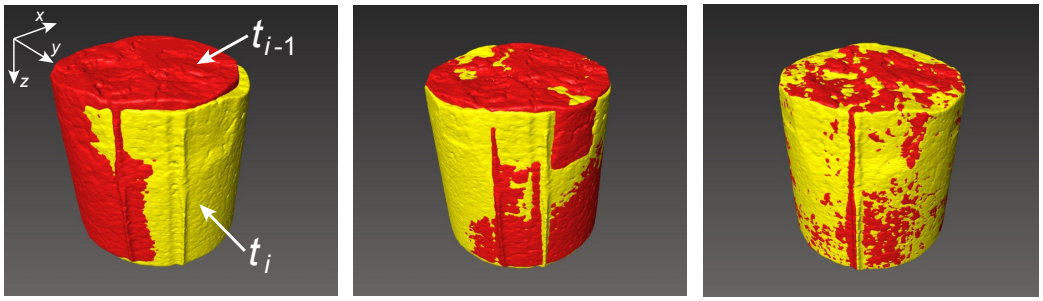

(a) (b) (c)

Figure 4: Elimination of sample misalignment between times t_{i-1} and t_i during a short-term annealing series: (a) original tomographic reconstructions; (b) after correction for translational offsets of the sample centroids; (c) following correction for both translational and rotational offsets.

step and operating backwards in time. The underlying strategy is to identify overlaps of particles between times t_i and t_{i-1}. For a given target particle having the size $R(t_i)$, we extract its 3D intersection with the segmented microstructure at time t_{i-1}. Within this region we search for candidate particles that could be the earlier-time manifestation of the target particle. Candidate particles are classified according to the relative change in equivalent particle radius during the one-hour anneal, $[R(t_i) - R(t_{i-1})]/R(t_i)$, with changes greater than $0.1[\langle R\rangle/R(t_i)]^2$ being rejected as unphysical (where $\langle R\rangle$ denotes the sample-averaged equivalent particle radius at time t_i). The normalization factor $[\langle R\rangle/R(t_i)]^2$ is introduced to permit larger relative size changes for smaller particles (as predicted, for instance, by the LSW model). If no candidate particle fulfills this criterion, or if more than one candidate does so, then the target particle is classified as untraceable.

3. Ostwald ripening results and discussion

Carrying out the image processing and segmentation steps outlined above, we were able to map out more than 2000 particles in the interior regions of each sample in the initial annealing state (1 h at 630°C). Evolution of the microstructure was then induced via a series of one-hour anneals (Table 1, ST series) or progressively longer heating intervals (Table 1, LT series). From the latter, we investigated the shape of the particle size distribution and the power-law growth of the average particle size, while the former measurements

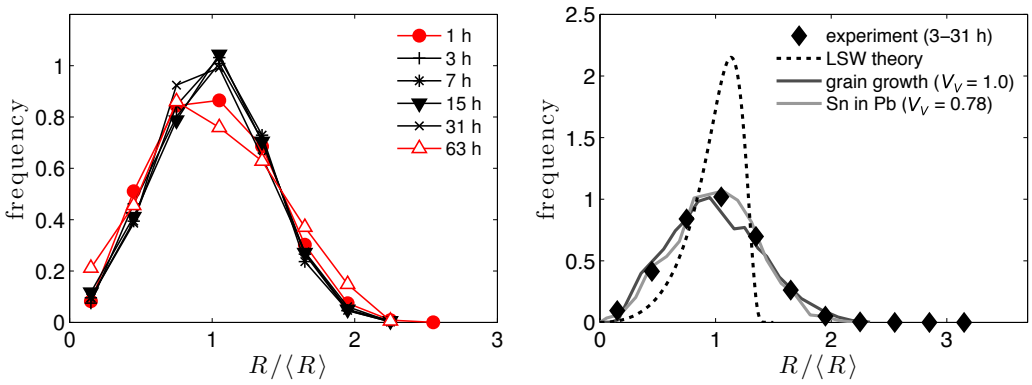

Figure 5: (a) Size distributions of interior particles (sum of samples LT1–6) plotted against the normalized particle radius $R/\langle R\rangle$ for each annealing time in the long-term annealing series of Al-5 wt% Cu. The size distribution appears to evolve self-similarly between annealing times of 3 and 31 h. (b) Comparison of Al-5 wt% Cu results (average of histograms from 3 to 31 h) to an experimental study of Ostwald ripening of Sn in Pb ($V_V = 0.78$) [37] and to a phase-field simulation of isotropic grain growth ($V_V = 1.0$) [38].

offered insight into the growth/shrinkage rates of individual particles.

3.1. Particle size distributions and growth exponent

Figure 5(a) illustrates the evolution of the particle size distribution (PSD) during the long-term annealing series; each histogram incorporates the particle sizes measured in all six samples, LT1 through LT6, normalized by the corresponding average particle radius $\langle R\rangle$, which increased monotonically from an initial value of 115 μm to about 240 μm at the longest annealing time of 63 h (Figure 6). The shape of the PSD appears to change somewhat between the annealing times of 1 h and 3 h; thereafter, the shape remains roughly constant—perhaps narrowing slightly in width—through 31 h. At 63 h, however, the PSD takes on a noticeably asymmetric shape having a greater width than at earlier times.

The invariance in distribution shape at intermediate times is consistent with self-similar evolution of the size distribution, as expected for Ostwald ripening in the asymptotic limit [12, 39]. The behavior between 1 and 3 h likely reflects a transient change from the PSD established by sample preparation to the distribution corresponding to self-similar coarsening. Computations performed by Chen and Voorhees [40] predict a decrease in duration

of the transient regime with increasing V_V, which could account for the rapid start of self-similar growth in our samples. The termination of self-similar evolution between 31 and 63 h likely arises from the fact that the average particle size begins to approach the smallest characteristic dimension of the sample itself (the cylinder diameter). As a result, a considerable fraction of particles touches the sample surface and cannot grow freely. This, in turn, affects the growth of nearby interior particles, tending to slow down the overall kinetics.

Comparing our data to the prediction of classical LSW theory [16, 17], which applies in the limit $V_V \to 0$, we observe that the PSD in Al-5 wt% Cu manifests a much broader and more symmetric shape (Figure 5(b)), which is in qualitative agreement with the trend revealed by both experiment [37, 41] and computer simulation [42, 43] for increasing V_V. In fact, the result of a 3D phase-field simulation of grain growth [38]—which could be viewed as the extreme case of $V_V = 1$—is significantly closer to the measured steady-state PSD of Al(Cu) particles than is the LSW distribution. Remarkably good agreement is found between the Al-5 wt% Cu results and serial-sectioning measurements of the particle size distribution following Ostwald ripening of Sn in Pb at $V_V = 0.78$ [37].

A plot of the cubed mean equivalent particle radius against annealing time reveals a nearly linear region between 3 h and 31 h (Figure 6), which is consistent with the above observation of self-similar evolution of the size distribution throughout this time interval. This linearity corresponds to a growth exponent of $n = 3$ in a power law of the form

$$[\langle R \rangle(t)]^n = [\langle R \rangle_0]^n + kt, \tag{1}$$

where $\langle R \rangle_0$ denotes the average particle radius at time $t = 0$, and k is a positive constant. Extraction of a more accurate value for n by fitting Equation (1) to the data for $\langle R \rangle(t)$ is hindered by the limited number of particle size determinations and by their narrow dynamic range. Nevertheless, it should be noted that $n = 3$ has been reported to hold for a wide variety of Ostwald ripening systems independently of V_V, based on the findings of experiment [37, 41], computer simulation [44] as well as analytic modeling [45, 46].

The data points at 63 h—which lie well below an extrapolation of the linear fit in Figure 6—reflect the influence of particle sizes approaching the smallest characteristic sample dimension, as discussed above. The spread in

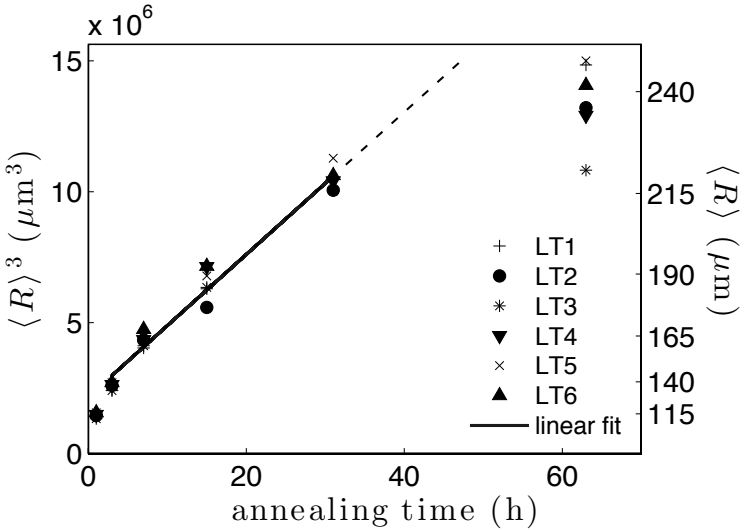

Figure 6: Cube of the mean equivalent particle radius in Al-5 wt% Cu plotted against annealing time at 630°C for the LT annealing series. The solid line represents a least-squares fit of a linear function to the data points between 3 and 31 h; the dotted line is an extrapolation of the linear fit to later annealing times.

initial average particle sizes of the LT samples is small ($\lesssim 2\%$ deviation from the average over six samples), and in all but one case the spread remains below $\sim 5\%$ at later annealing times, indicating not only the presence of statistically similar starting microstructures but also highly reproducibile coarsening kinetics. The outlier for sample LT3 at 63 h can be attributed to poor contrast in the tomographic scan, which led to boundary segmentation errors in parts of the microstructure.

3.2. Particle trajectories and growth rates

In order to track the evolution of individual particles during short-term (ST) anneals, it was necessary to align the segmented microstructures with respect to a common coordinate system, following the procedure described in Section 2.3. In Figure 7 we map out all particles in sample ST1 that could be tracked over the entire annealing interval between 3 and 7 h; each particle's color is indexed to its label, facilitating the identification of the same particle in each data set. Examples for a growing (red) and a shrinking (green) particle are highlighted. As a measure for the reliability of the tracking algorithm, we define the efficiency $\eta(t_i)$ as the ratio of the number of traceable

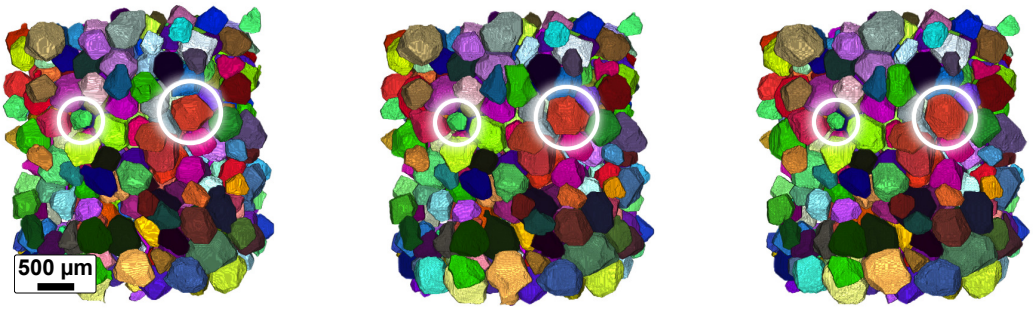

(a) 3 hours (b) 5 hours (c) 7 hours

Figure 7: Visualization of tracked particles in annealing series ST1 over a four-hour time interval. The circles enclose a shrinking (green) and a growing (red) particle.

particles between time steps t_i and t_{i-1} to the total number of particles segmented at time t_i. During early stages of microstructural evolution (*e.g.* annealing series ST1), particle sizes are small and the corresponding growth rates are high: under such conditions, our particle tracking routine had a mean efficiency of approximately 84% (Figure 8). As the average particle size increased and the overall growth rate slowed, the tracking efficiency rose to 94% for annealing series ST2 and to 98% for series ST3.

The ability to follow the size evolution of individual particles opens up new avenues for investigating Ostwald ripening that are well beyond the scope of conventional techniques. For example, particle size trajectories can now be plotted for individual particles in a sample, as illustrated in Figure 9. In contradiction to prediction (iii) of the LSW model (Section 1), some particles that are larger than the overall mean particle size are found to shrink over time, and some particles smaller than $\langle R \rangle$ grow. Additionally, the fact that trajectories in some instances were observed to cross implies that a given particle's size class cannot be the only factor determining whether the particle shrinks or grows. Similar observations were reported for computer simulations of Ostwald ripening at $V_V = 0.35$ [47] and even for experiments performed at $V_V = 0.03$ [48].

Plotting the quantity $R^2 \mathrm{d}R/\mathrm{d}t$ against the normalized particle size illustrates the discrepancy between experiment and theory even more clearly (Figure 10). In the LSW model, the particle growth rate scales strictly linearly with $R/\langle R \rangle$, changing sign when $R = \langle R \rangle$. Not only do the measured particle growth rates take on a wide range of values for particles in

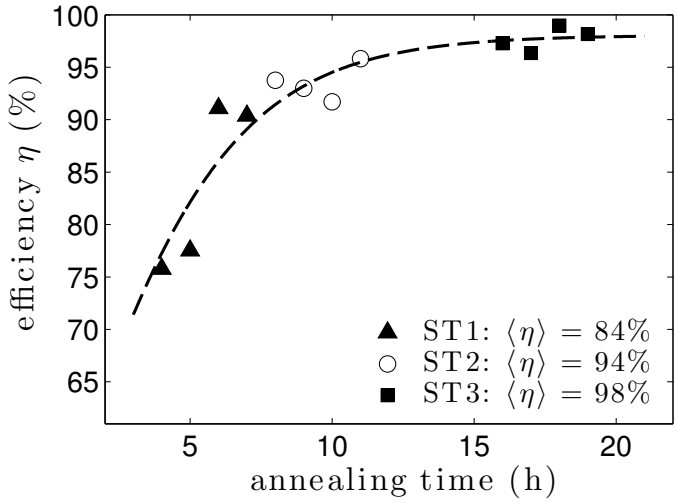

Figure 8: Efficiency of particle-tracking algorithm with increasing annealing time. The mean efficiency $\langle\eta\rangle$ is computed by averaging the values obtained over one-hour time intervals within each short-term (ST) annealing series. The dashed curve is a least-squares fit of a sigmoid function to the data points.

the same size class, but the cloud of data points manifests an upward curvature rather than the predicted linearity. Both of these experimental findings are consistent with computer simulation and analytical modeling for $V_V > 0$ [23, 49, 50].

Because tomographic characterization and subsequent segmentation yields a complete mapping of the sample microstructure over time, it is possible to mine the data for clues to the underlying causes of phenomena like the scatter in growth rates within a given size class. Consideration of local mass conservation during the growth and shrinkage of particles suggests that the determining factor for a change in radius R of a given particle is not its relationship to the sample-averaged particle size $\langle R\rangle$ but rather to the average size of particles with which the diffusive exchange of atoms is likely to take place: namely, with particles in the immediate vicinity of the particle of size R [18, 50]. We denote the mean size of nearest-neighbor particles as $\langle R\rangle_{\text{local}}$ and use this quantity to color code the data points in Figure 10 according to whether $R/\langle R\rangle_{\text{local}}$ is larger or smaller than unity. Inspection of this figure reveals that a particle usually gives up atoms to its surroundings if $R < \langle R\rangle_{\text{local}}$, even when R is simultaneously larger than $\langle R\rangle$ (in which case particle growth would be expected according to LSW). Likewise, $R > \langle R\rangle_{\text{local}}$

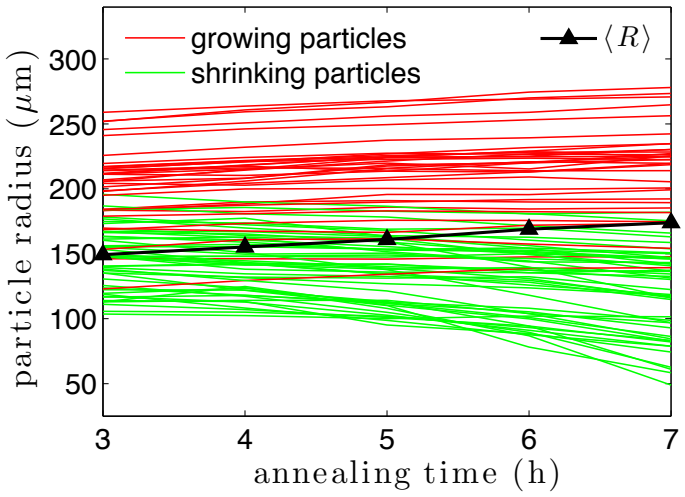

Figure 9: Particle trajectories illustrating the evolution in equivalent radius R of randomly chosen particles in Al-5 wt% Cu during annealing series ST1. Red curves denote growing and green curves shrinking particles. For comparison, the sample-averaged mean particle radius $\langle R \rangle$ is plotted at each time step with black triangles.

is usually a telltale indicator for particle growth, even in the rare occasion that R happens to be smaller than $\langle R \rangle$. The non-negligible frequency with which these "rules" are violated, however, indicates that the $R/\langle R \rangle_{\mathrm{local}}$ ratio cannot account for all of the scatter in Figure 10—apparently, additional factors must also be considered in order to capture the underlying physics of coarsening in Al-5 wt% Cu at $V_V = 0.74$.

4. Evaluation of experimental procedures and data analysis

We now assess the accuracy of the microstructural information extracted from tomographic reconstructions of Al-5 wt% Cu according to the procedures described in the previous sections. After briefly considering the limitations imposed by the *ex situ* manner in which the data were collected, we discuss the origin of segmentation errors and the extent to which they affect the efficiency of the particle-tracking routine.

4.1. Ex situ data collection

In this study, we performed tomographic characterization *ex situ* to the thermal treatment that induced Ostwald ripening. Chief among the many

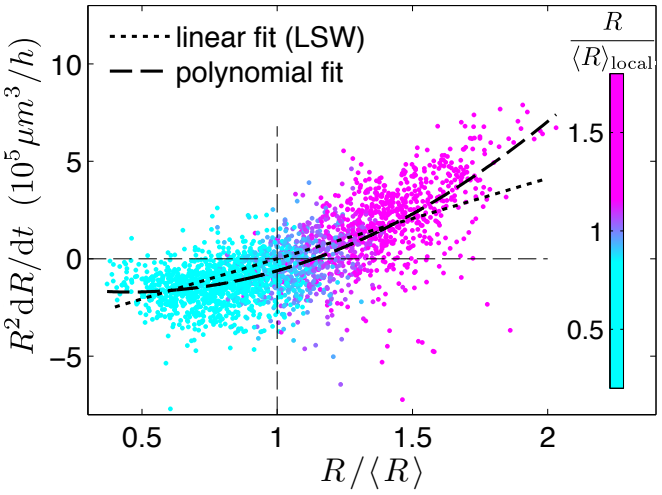

Figure 10: Scaled growth rates of individual particles in Al-5 wt% Cu (annealing series ST1) compared to the prediction of LSW theory. The color map is indexed to the equivalent radius R of each particle normalized to the average size of its nearest neighbors, $\langle R\rangle_{\mathrm{local}}$.

practical advantages inherent to this approach is its compatibility with commercial tabletop x-ray tomographs as used in this work, which typically do not provide sufficient space for an oven capable of heating centimeter-sized specimens above a few hundred degrees Celsius. Even if an oven could be inserted into such a tomograph, the tight quarters would make it challenging to avoid the generation of thermal gradients across the sample. In the much larger confines of a tube or chamber furnace, however, it is straightforward to establish a homogeneous temperature profile over the entire sample volume. The uniformity of the resulting microstructural evolution is further supported by presence of the high-V_V solid phase, which forms a stable skeletal structure that effectively suppresses convection and sedimentation effects [51]. Even after annealing treatments of 63 h duration, there was no evidence for gravitation-induced inhomogeneities in the sample microstructure.

These advantages of the *ex situ* approach must be weighed against two significant drawbacks, both related to the microstructural changes that occur during the sample quench from the annealing state to room temperature, Figure 2. As the sample temperature drops, the volume fraction of the liquid phase decreases, which is accommodated at least partially through the migration of solid particle boundaries into the region occupied by liquid;

consequently, the solid particles grow slightly in size during the cooling step. Moreover, once the eutectic temperature is crossed, the remaining liquid crystallizes into two solid phases, only one of which (Al_2Cu) provides absorption contrast for x-ray photons relative to the coarsening phase. If the "layer" of Al_2Cu decorating a particle boundary is thin (say, below the effective voxel side length of 4 µm after downsampling), then there is an increased likelihood for tomography to fail to detect the boundary. And even if the boundary is observed, we do not know how much thicker the corresponding liquid layer actually was during coarsening. The best we can do is to note that the uniform boundary widening step carried out in Section 2.1 resulted in a final boundary thickness of 12 µm to 24 µm, which corresponds to a maximum particle radius increase of 6 µm to 12 µm. Since $\langle R \rangle$ in Al-5 wt% Cu grows from 115 µm to about 240 µm over the course of a long-term anneal, the cooling-induced change in radius is on the order of only 5% for particles of average size. The latter value could be reduced significantly by drastically increasing the cooling rate from 630°C to room temperature, thereby giving the solid phase insufficient time to grow into the liquid region [52]. It should be noted, however, that rapid quenching techniques like immersion in an oil or water bath typically generate high stresses that must be counteracted by a protective sample layer; otherwise, significant sample deformation may ensue.

Finally it should be mentioned that it would have been feasible to investigate somewhat larger Al-Cu samples than the ones employed in this study. Frequently, the limiting dimension in x-ray tomography is the sample diameter, as a sample must be thin enough at all projection angles for a sufficiently high fraction of the incident x-ray intensity to reach the detector. When measured in a Skyscan 1172 tomograph, the practical maximum sample diameter for Al-5 wt% Cu is on the order of 6 mm. Although such specimens would have contained a significantly greater number of grains than did the samples investigated in this study, the resulting measurement times would have been longer, and the increased number of particles would have rendered the tasks of image segmentation, data analysis and particle tracking correspondingly more complex.

4.2. Segmentation and particle tracking

The processing and quantitative analysis of a large number of tomographic reconstructions—as in the present study—is practically feasible only with the help of an automated segmentation algorithm like the one described

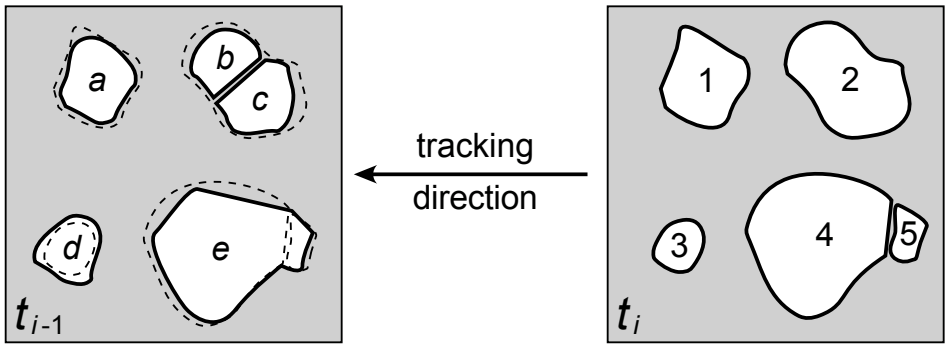

Figure 11: Schematic representation of segmentation errors and their relevance to particle tracking from time step t_i to time step t_{i-1}. *Oversegmentation:* particle 2 is incorrectly represented as particles *b* and *c*. *Undersegmentation:* particles 4 and 5 are incorrectly represented as single particle *e*. *Traceable particles:* in the calculation of the tracking efficiency η, only particles 1 and 3 will be classified as traceable, since the apparent change in relative size of particles 2, 4 and 5 exceeds the threshold criterion. In the sketch at time t_{i-1}, the dashed curves illustrate the corresponding particle boundaries at t_i.

in Section 2.1. This raises the issue of validation: How accurate are the particle boundaries extracted by this approach? A statistical test for validity can be carried out by comparing our segmentation results to previously reported data for Ostwald ripening at high volume fractions of the coarsening phase. As discussed in Section 3.1, both the value for the growth exponent and the shape of the particle size distribution in Al-5 wt% Cu are consistent with literature data obtained from conventional—usually manual—image processing and analysis routines.

A more stringent test for segmentation validity arises as a natural byproduct of the particle trajectory determination carried out in Section 3.2. There, an efficiency parameter η was defined to quantify the fraction of particles that could be tracked successfully (in reverse) across a one-hour annealing interval. Not surprisingly, η was found to improve at longer annealing times, where the average particle size is larger and the average growth rate smaller. (The smaller the relative change in particle size, the greater is the overlap between respective particle volumes prior to and following the annealing interval.) But more enlightening from the standpoint of validation are the instances in which tracking fails, particularly when the underlying cause for failure can be traced to a segmentation error.

Indeed, an inspection of data sets at both early and later annealing times revealed that virtually all ambiguities in particle tracking could be attributed

to either oversegmentation or undersegmentation errors. *Oversegmentation* denotes the incorrect division of the region occupied by a single particle into two or more subvolumes. This phenomenon is most likely to occur when the particle in question has an elongated shape (especially if the overall microstructure is otherwise equiaxed), as the segmentation algorithm may incorrectly pass a boundary from one side of the particle to the other, thereby splitting it into two. A schematic illustration of oversegmentation is given in Figure 11, where the boundary between particles b and c at time step t_{i-1} is superfluous; in reality, subvolumes b and c belong to the region occupied by a single particle (evident as particle 2 at time step t_i).

Undersegmentation, on the other hand, occurs when a boundary between particles is erroneously left out of the segmentation. As a result, two or more particles are incorrectly subsumed into a single particle. This segmentation error is particularly prevalent when a small particle is located next to a much larger particle: if the segmentation algorithm fails to detect the boundary separating them, then the smaller and larger particles will be joined together, as illustrated in Figure 11 by particle e.

In most cases, each of these segmentation errors causes a violation of the traceability criterion imposed during particle tracking (Section 3.2). Thus, counting the number of untraceable particles during reverse tracking from t_i to t_{i-1} gives an upper bound on the number of over/undersegmentations in *either* time step. Assuming that the segmentation errors are roughly equally distributed between the two time steps, we can estimate the fraction of incorrectly segmented grains in any given segmentation to be $(1 - \eta)/2$. According to Figure 8, the latter quantity takes on a value of 0.1 at early annealing times (series ST1), but it drops rapidly to 3% for series ST2 and to 1% for series ST3. Since tracking ambiguities can be caused not only by segmentation errors but also by rapid changes in a particle's volume (such as those associated with the accelerated shrinking phase that generally sets in just prior to particle annihilation), it is plausible that the true probability for over/undersegmentation could be on the order of only one to two percent even for the early-time series ST1, as the latter is marked by the fastest rate of microstructural change. It should be noted that our segmentation error rate estimation implicitly assumes that over/undersegmentation occurs independently from time step to time step. Visual inspection of datasets confirmed the validity of this assumption, finding that segmentation errors rarely occur at the same boundary before and after a single annealing step (presumably because the microstructural changes that occur during one-hour annealing

intervals are large enough to alter the local conditions that contributed to over/undersegmentation).

5. Conclusions

In this work, x-ray computed tomography is found to be a powerful tool for the nondestructive investigation of Ostwald ripening at high volume fractions of the coarsening phase. Long-term annealing sequences yielded global measures for microstructural evolution, such as the growth exponent and the particle size distribution, which are in excellent agreement with previous studies of Ostwald ripening in similar systems. From short-term annealing series we gained access to local features of microstructural evolution, like the growth and shrinkage rates of individual particles; such data are completely inaccessible to conventional metallographic techniques for 3D characterization, as the latter destroy the sample. Automated image processing and segmentation routines were developed to close gaps in the particle boundary network, to extract particle volumes and to track individual particles from one time step to the next. Unexpectedly, the particle tracking efficiency—the likelihood that a particle present at a later time step t_i could be identified successfully in a segmentation of the earlier time step t_{i-1}—provided a quantitative means for validating the image processing and segmentation routines, as erroneous particle boundary placement invariably results in one or more particle tracking errors.

6. Acknowledgments

The authors are most grateful to D. Molodov of the Institute of Physical Metallurgy and Metal Physics, RWTH Aachen, for providing all Al-5 wt% Cu specimens and to the Deutsche Forschungsgemeinschaft for funding through NSF/DFG Materials World Network Project KR 1658/4-1.

References

[1] Salvo L, Cloetens P, Maire E, Zabler S, Blandin JJ, Buffière JY, et al. X-ray micro-tomography an attractive characterisation technique in materials science. Nucl Instrum Meth B 2003;200:273–86.

[2] Baruchel J, Buffière JY, Cloetens P, Michiel MD, Ferrie E, Ludwig W, et al. Advances in synchrotron radiation microtomography. Scripta Mater 2006;55:41–6.

[3] Kastner J, Harrer B, Degischer HP. High resolution cone beam X-ray computed tomography of 3D-microstructures of cast Al-alloys. Mater Charact 2011;62:99–107.

[4] Rowenhorst DJ, Voorhees PW. Measurement of interfacial evolution in three dimensions. Annu Rev Mater Res 2012;42:105–24.

[5] Alkemper J, Voorhees PW. Quantitative serial sectioning analysis. J Microsc 2001;201:388–94.

[6] Maire E, Buffière JY, Salvo L, Blandin JJ, Ludwig W, Létang JM. On the application of X-ray microtomography in the field of materials science. Adv Eng Mater 2001;3:539–46.

[7] Limodin N, Salvo L, Sury M, DiMichiel M. In situ investigation by X-ray tomography of the overall and local microstructural changes occurring during partial remelting of an Al–15.8 wt.% Cu alloy. Acta Mater 2007;55:3177–91.

[8] Zabler S, Rueda A, Rack A, Riesemeier H, Zaslansky P, Manke I, et al. Coarsening of grain-refined semi-solid AlGe32 alloy: X-ray microtomography and in situ radiography. Acta Mater 2007;55:5045–55.

[9] Terzi S, Salvo L, Suery M, Dahle A, Boller E. In situ microtomography investigation of microstructural evolution in Al-Cu alloys during holding in semi-solid state. T Nonferr Metal Soc 2010;20, Supplement 3:734–8.

[10] Aagesen LK, Fife JL, Lauridsen EM, Voorhees PW. The evolution of interfacial morphology during coarsening: A comparison between 4D experiments and phase-field simulations. Scripta Mater 2011;64:394–7.

[11] Ostwald W. Über die vermeintliche Isomerie des roten und gelben Quecksilberoxyds und die Oberflächenspannung fester Körper [On the assumed isomerism of red and yellow mercury oxide and the surface tension of solid particles]. Z Phys Chem 1900;34:495–503.

[12] Ratke L, Voorhees PW. Growth and coarsening—Ripening in materials processing. Springer Verlag, Berlin; 2002.

[13] German RM, Suri P, Park S. Review: Liquid phase sintering. J Mater Sci 2009;44:1–39.

[14] Taylor P. Ostwald ripening in emulsions. Adv Colloid Interfac 1998;75:107–63.

[15] Vengrenovich R, Gudyma Y, Yarema S. Ostwald ripening of quantum-dot nanostructures. Semiconductors 2001;35:1378–82.

[16] Lifshitz IM, Slyozov VV. The kinetics of precipitation from supersaturated solid solutions. J Phys Chem Solids 1961;19:35–50.

[17] Wagner C. Theorie der Alterung von Niederschlägen durch Umlösen (Ostwald-Reifung) [Theory of the aging of precipitates by dissolution-reprecipitation (Ostwald ripening)]. Z Elektrochem 1961;65:581–91.

[18] Ardell AJ. The effect of volume fraction on particle coarsening: Theoretical considerations. Acta Metall Mater 1972;20:61–71.

[19] Akaiwa N, Voorhees PW. Late-stage phase separation: Dynamics, spatial correlations, and structure functions. Phys Rev E 1994;49:3860–80.

[20] Ardell AJ, Nicholson RB. The coarsening of γ' in Ni-Al alloys. J Phys Chem Solids 1966;27:1793–4.

[21] Hardy SC, Voorhees PW. Ostwald ripening in a system with a high volume fraction of coarsening phase. Metall Mater Trans A 1988;19:2713–21.

[22] Davies CKL, Nash P, Stevens RN. The effect of volume fraction of precipitate on Ostwald ripening. Acta Metall Mater 1980;28:179–89.

[23] Marsh SP, Glicksman ME. Kinetics of phase coarsening in dense systems. Acta Mater 1996;44:3761–71.

[24] Glicksman ME, Wang KG, Marsh SP. Diffusional interactions among crystallites. J Cryst Growth 2001;230:318–27.

[25] Kadanoff LP. More is the same; Phase transitions and mean field theories. J Stat Phys 2009;137:777–97.

[26] Wang KG, Glicksman ME, Rajan K. Modeling and simulation for phase coarsening: A comparison with experiment. Phys Rev E 2004;69:061507.

[27] Wang K, Ding X, Chang K, Chen LQ. Phase-field simulation of phase coarsening at ultrahigh volume fractions. J Appl Phys 2010;107:061801.

[28] Voorhees PW. The theory of Ostwald ripening. J Stat Phys 1985;38:231–52.

[29] Massalski T. Binary alloy phase diagrams—AlCu phase diagram; vol. 1. 3rd ed.; ASM International, Materials Park, Ohio; 1996, p. 141–3.

[30] Aravind M, Yu P, Yau MY, Ng DHL. Formation of Al_2Cu and AlCu intermetallics in Al(Cu) alloy matrix composites by reaction sintering. Mat Sci Eng A 2004;380:384–93.

[31] Annavarapu S, Doherty RD. Inhibited coarsening of solid-liquid microstructures in spray casting at high volume fractions of solid. Acta Metall Mater 1995;43:3207–30.

[32] Niemi A, Courtney T. Microstructural development and evolution in liquid-phase sintered Fe-Cu alloys. J Mater Sci 1981;16:226–36.

[33] Williams WM, Smith CS. A study of grain shape in an aluminum alloy and other applications of stereoscopic microradiography. J Metals 1952;167:755–65.

[34] Brunke O, Odenbach S, Beckmann F. Quantitative methods for the analysis of synchrotron-μCT datasets of metallic foams. Eur Phys J Appl Phys 2005;29:73–81.

[35] Weickert J. Anisotropic diffusion in image processing. B.G. Teubner, Stuttgart; 1998.

[36] Russ JC. The Image Processing Handbook. 5th ed.; CRC Press, Boca Raton, Florida; 2007.

[37] Rowenhorst DJ, Kuang JP, Thornton K, Voorhees PW. Three-dimensional analysis of particle coarsening in high volume fraction solid-liquid mixtures. Acta Mater 2006;54:2027–39.

[38] Krill III CE, Chen LQ. Computer simulation of 3-D grain growth using a phase-field model. Acta Mater 2002;50:3057–73.

[39] Groza JR, Shackelford JF, Lavernia EJ, Powers MT. Materials processing handbook. 1st ed.; CRC Press, Boca Raton, Florida; 2007, p. 5–1.

[40] Chen MK, Voorhees PW. The dynamics of transient Ostwald ripening. Model Simul Mater Sci 1993;1:591–612.

[41] Bender W, Ratke L. Ostwald ripening of liquid phase sintered Cu-Co dispersions at high volume fractions. Acta Mater 1998;46:1125–33.

[42] Baldan A. Progress in Ostwald ripening theories and their applications to nickel-base superalloys part I: Ostwald ripening theories. J Mater Sci 2002;37:2171–202.

[43] Kim SG. Large-scale three-dimensional simulation of Ostwald ripening. Acta Mater 2007;55:6513–25.

[44] Fan D, Chen SP, Chen LQ, Voorhees PW. Phase-field simulation of 2-D Ostwald ripening in the high volume fraction regime. Acta Mater 2002;50:1895–907.

[45] Voorhees PW. Ostwald ripening of two-phase mixtures. Annu Rev Mater Res 1992;22:197–215.

[46] Wang K, Glicksman M, Rajan K. Length scales in phase coarsening: theory, simulation, and experiment. Comp Mater Sci 2005;34:235–53.

[47] Voorhees PW, Glicksman ME. Solution to the multi-particle diffusion problem with applications to Ostwald ripening—II. Computer simulations. Acta Metall Mater 1984;32:2013–30.

[48] Voorhees PW, Schaefer RJ. *In situ* observation of particle motion and diffusion interactions during coarsening. Acta Metall Mater 1987;35:327–39.

[49] Voorhees PW, Glicksman ME. Ostwald ripening during liquid phase sintering—Effect of volume fraction on coarsening kinetics. Metall Mater Trans A 1984;15:1081–8.

[50] Wang K, Glicksman ME, Lou C. Correlations and fluctuations in phase coarsening. Phys Rev E 2006;73:061502.

[51] Akaiwa N, Hardy SC, Voorhees PW. The effects of convection on Ostwald ripening in solid-liquid mixtures. Acta Metall Mater 1991;39:2931–42.

[52] Pompe O, Rettenmayr M. Microstructural changes during quenching. J Cryst Growth 1998;192:300–6.